Fluorescence-detected multidimensional electronic spectroscopy

Amitav Sahu, Vivek Nagendra Bhat, Sanjoy Patra and Vivek Tiwari

Solid State and Structural Chemistry Unit, Indian Institute of Science, Bangalore-560 012, India

Multidimensional electronic spectroscopy (MES) is a state-of-the-art spectroscopic tool which provides two-dimensional (2D) contour map snapshots of ultrafast quantum dynamics with high temporal and spectral resolution. However, limited sensitivity of interferometric detection in the presence of scatter and lack of spatial resolution limits our understanding of several open questions, such as morphology dependence of exciton dissociation and photocurrent efficiency in photovoltaic thin films, and pure decoherence lifetimes on excited state coherences in photosynthetic proteins without ensemble averaging. We report a home-built fluorescence-detected MES (fMES) spectrometer based on a visible white-light continuum which overcomes the sensitivity and spatial resolution limitations of conventional MES. Our spectrometer is integrated with a confocal microscope to provide spatial resolution limited by the microscope objective. As a demonstration of sensitivity enhancement, we report high signal-to-noise ratio 2D coherence maps (CMs) which isolate vibrational coherences on the excited and ground electronic states of a laser dye based on the phase of vibrational quantum beats, at optical densities ~10× lower than what is typical for conventional MES approaches. © Anita Publications. All rights reserved.

Keywords: Coherences, Solvation, Fluorescence, Wavepackets, Femtosecond.

1 Introduction

Multidimensional electronic spectroscopy (MES) [1], an optical analog [2,3] of multidimensional nuclear magnetic resonance, has provided unprecedented mechanistic details of ultrafast quantum dynamics of energy and charge transfer in a variety of systems spanning photosynthetic proteins [4,5] to photovoltaic materials [6-8]. A MES experiment correlates the excitation and detection frequencies of a system in the form of a 2D contour map. The 2D electronic spectra (2DES) evolve along the pump-probe waiting time T and spectrally decongest ultrafast solvation, energy, or charge transfer dynamics along three spectral dimensions-excitation, detection, and coherence frequency axes along with routine sub-10fs temporal resolution. Fourier transformation of coherent dynamics along T obtains the coherence frequency axis.

Briefly, a typical MES experiment involves three precisely controlled light-matter interactions which generate a third-order oscillating non-linear macroscopic polarization $\hat{P}^{(3)}(t; t_1; t_2; t_3)$ in the sample. Here, t_{1-3} represent the experimentally controllable pulse envelope centers. The first and third interactions generate an optical coherence. The optical coherence after the first interaction is sampled by scanning the envelope or carrier-wave time-delay τ between the first two pulses with interferometric stability. Fourier transform of the first optical coherence along τ results in the excitation frequency axis ω_τ. The optical coherence after the third interaction is typically detected via homodyne or heterodyned spectral interferometry resulting in the detection frequency axis ω_t. The time-ordering of pulses can control the phase of the optical coherences generated after the first and third interactions. A rephasing or a photon-echo pulse sequence reverses the phase of optical coherence during the third time-interval, while a non-rephasing pulse sequence does not. The frequency resolution of such an experiment is only limited by the optical dephasing time scale of the system,

---

Corresponding author
e mail: vivektiwari@iisc.ac.in (Vivek Tiwari)

and simultaneous femtosecond temporal resolution is possible along the pump-probe waiting time T, that is, the time-delay between the 2nd and 3rd pulses. A key point about the MES experiment is that the coherent and population dynamics of multiple vibration-electronic states resulting from impulsive pump excitations can now be decongested along the excitation frequency axis which is not possible in a impulsive pump-probe experiment.

The non-linear polarization $\hat{P}^{(3)}(t; t_1; t_2; t_3)$ radiates a signal field in a specific phase-matched direction $\vec{k}_{sig}$ determined by the input wavevectors. For example, along a particular phase-matched direction $\vec{k}_{sig} = -\vec{k}_1 + \vec{k}_2 + \vec{k}_3$, the subscripts 1 – 3 label the input electric fields. Direction filtering of radiated signal followed by heterodyne is advantageous because of its background free nature. However, this necessarily requires the experimental geometry to be non-collinear, therefore, limiting the possibility of microscope objective limited spatial resolution. Further, heterodyne detection becomes challenging in the presence of pump-scatter, for example, when probing [9] *in-vivo* photosynthetic energy transfer. Crucially, in the typically employed BoxCARS geometry, the sample volume covered by the focal spot sizes should be several times larger than the wavelength of light for an efficient pump grating diffraction efficiency. These above limitations imply that the sensitivity and spatial resolution of MES is limited. Because of sensitivity and spatial resolution limitations questions such as the dependence of local morphology on exciton dissociation rates [10] or pure dephasing rates of coherences along T in the presence of energetic averaging [5] are not directly accessible to MES experiments.

In an alternate approach to MES, first demonstrated by Warren and co-workers [11], the third-order non-linear oscillating polarization is projected on the excited electronic state to create a fourth-order population by using an additional pulse in the experiment. In such an approach, the four pulses can be collinear and the resulting non-linear population can be detected [12] as fluorescence, photocurrent or photoelectrons. Since directional filtering is no longer possible in a collinear geometry, the non-linear signal is isolated from linear signals using static [11,13,14] or dynamic [15] phase cycling. Tekavec *et al* demonstrated [15] a acousto-optic phase modulation (AOPM) approach, where the carrier-envelop phase of each of the four pulses is dynamically phase-cycled at a unique radio frequency for every laser shot, and the resulting non-linear fluorescence signal is frequency-filtered using phase-sensitive lock-in detection. Fluorescence-detected MES (fMES) has been naturally extended to spatially-resolved measurements in the near-IR wavelength region [16,17] to combine spatial, spectral and temporal resolutions.

We present a white light continuum-based home-built fMES spectrometer that spans the visible wavelength spectral region. The spatial resolution of our spectrometer is microscope objective limited, with spectral bandwidth corresponding to sub-15fs transform limited temporal resolution. We demonstrate enhanced sensitivity of fluorescence-detection by collecting rephasing and non-rephasing 2DES spectra with high signal-to-noise ratio at optical densities as low as ~0.02, an order of magnitude lower than what is typical in conventional MES. Enhanced detection sensitivity allows us to resolve weak room-temperature vibrational coherences in a laser dye in the form of 2D coherence maps. Phase analysis of the vibrational quantum beats allows us to disentangle ground versus excited electronic state vibrational coherences demonstrating the rich information content available in a multidimensional spectroscopy experiment. This represents the first implementation of fMES based on a broadband visible white-light continnum at repetition rates down to 1 MHz, where a combination of visible white light continuum and lower repetition rates present specific sets of challenges not present in near IR, or non-white-light based approaches at higher repetition rates.

2 Theory

A fMES experiment can be interpreted as an extension of fluorescence-detected wavepacket interferometry experiments pioneered by Scherer *et al* [18]. In a fMES experiment, wavepacket amplitudes

resulting from various orders of time-delayed light-matter interactions interfere to result in modulation of excited state fluorescence as a function of time delays t_{12}, t_{23} or T and t_{34} depicted in Fig 1. This formalism has been detailed by Cina [19] and Tekavec *et al* [15], and will be briefly outlined here. For a two-level system with two electronic states $|g\rangle$, $|e\rangle$, where $|g\rangle$ is the initial state (at $t = 0$), the time-dependent first-order perturbation results a state, $|\psi^{(1)}(t)\rangle = -\dfrac{i}{\hbar} \int_0^t |e\rangle\ e^{-\omega_e(t-t')}\ (-\hat{\mu}_{eg}.\ \vec{E}(t'))\ e^{-i\omega_g(t')}\ dt'$. This integral can be converted [1] into a Fourier transform such that a first order light-matter interaction transfers a probability amplitude of $\dfrac{i}{\hbar}\ \vec{\mu}_{eg}.\vec{E}(\omega_{eg})$ to the excited state $|e\rangle$. The fourth order non-linear population in the fMES experiment is generated by four such interactions, one each from electric fields labeled 1–4, and given by time-dependent interference of wavepacket overlaps such as $\langle\psi^{(3)}_{acd}\ |\ \psi^{(1)}_b\rangle$ and $\langle\psi^{(3)}_{abd}\ |\ \psi^{(1)}_c\rangle$, corresponding to rephasing excited state emission (ESE) and ground state bleach (GSB) signal pathways, respectively. In the same fashion wavepacket overlap such as $\langle\psi^{(1)}_a|\psi^{(1)}_b\rangle$ lead to linear fluorescence signal. Overall, the total fluorescence is time-integrated by the detector and depends [1] on a cyclic product of four transition dipoles, a spectral filter generated by the product of four electric fields, and time delay between different pulses in the experiment.
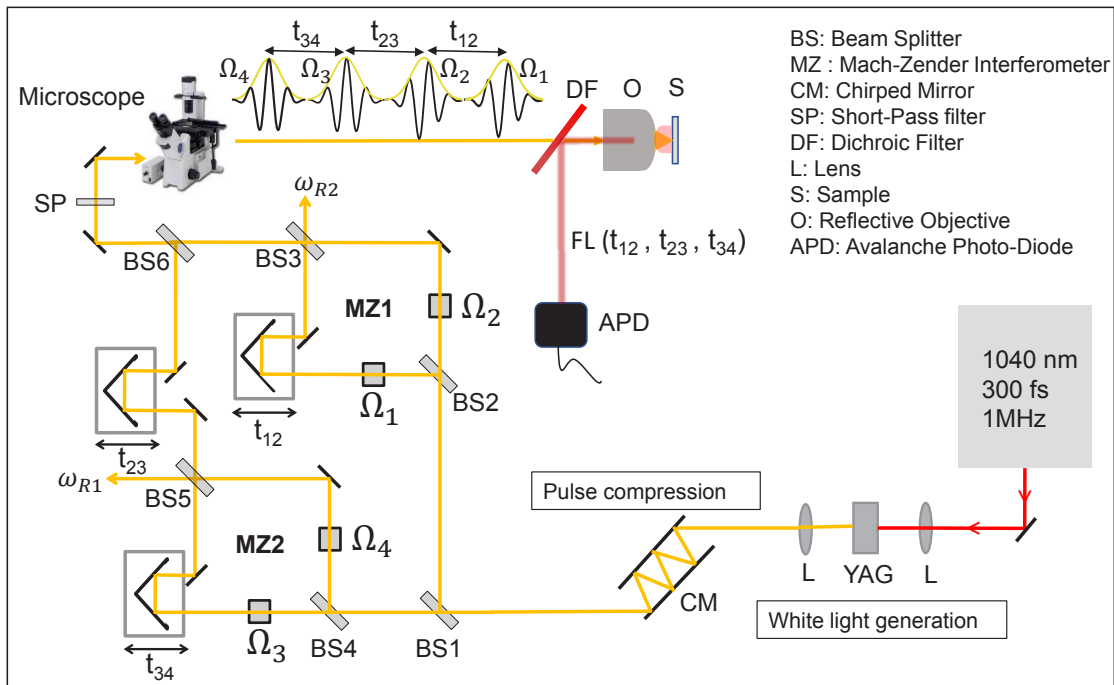
Fig 1. Experimental schematic of the fMES spectrometer setup. Experimentally controllable carrier envelopephase imparted by the AOMs and the time delays between the collinear pulses are also shown.

In the AOPM approach, the carrier-envelope phase of electric fields 1-4 is tagged with a unique radio frequency Ω_{1-4} which is cycled for successive laser pulses. This phase modulation at Ω_{1-4} leads to amplitude modulation of the interfering wavepackets, resulting in sum and difference radio frequency combinations corresponding to non-rephasing and rephasing signals. That is, $\Omega_- = -\Omega_{12} + \Omega_{34}$ and $\Omega_+ = \Omega_{12} + \Omega_{34}$ correspond to rephasing and non-rephasing signal frequencies, where $\Omega_{ij} = \Omega_i - \Omega_j$. The modulating fluorescence signals

are demodulated using a reference based phase-sensitive lock-in detection [15] described in the Section 3. Briefly, detection relative to an optically generated reference, ω_{R1} and ω_{R2} from each interferometer, the optical coherence during time delays t_{12} and t_{34} is down sampled at frequency $\omega_{eg} - \omega_{R1:2}$. This has two vital advantages-passive phase stabilization through minimized susceptibility to phase-instabilities, and ability to physically under sample optical coherences leading to increased throughput.

In order to understand the results discussed in Section 3, it is helpful to briefly revisit the 2D CM analysis which is routinely employed [5] to decipher the origin of coherent signals in MES and the mechanistic details of the photophysics leading to such signals. We start with the response function formalism [1] such that the third-order response functions can be written as a product of three Green's functions for describing time evolution along the three time-intervals and a product of four transition dipoles, one for each light-matter interaction. Applying the formalism for a two electronic level system with vibrational quanta $v = 0, 1$ on each electronic level, and setting $\hbar = 1$; a rephasing GSB vibrational coherence response pathway can be written as

$$R^{GSB}(t_{12}, t_{23}, t_{34}) = \left\langle \left(\vec{\mu}_{g_0 e_0} \cdot \vec{E}_a \right) \left(\vec{\mu}_{e_0 g_1} \cdot \vec{E}_b \right) \left(\vec{\mu}_{e_1 g_0} \cdot \vec{E}_c \right) \left(\vec{\mu}_{g_1 e_1} \cdot \vec{E}_d \right) \right\rangle_{orientational}$$
$$\times \left\langle G_{g_0 e_0}(t_{12}) \, G_{g_0 g_1}(t_{23}) \, G_{e_1 g_1}(t_{34}) \, \rho_{g_0 g_0} \right\rangle_{ensemble}. \tag{1}$$

In the same fashion, response function pathway leading to rephasing ESE vibrational coherences can be written as –

$$R^{ESE}(t_{12}, t_{23}, t_{34}) = \left\langle \left(\vec{\mu}_{g_0 e_0} \cdot \vec{E}_a \right) \left(\vec{\mu}_{e_1 g_0} \cdot \vec{E}_b \right) \left(\vec{\mu}_{e_0 g_1} \cdot \vec{E}_c \right) \left(\vec{\mu}_{g_1 e_1} \cdot \vec{E}_d \right) \right\rangle_{orientational}$$
$$\times \left\langle G_{g_0 e_0}(t_{12}) \, G_{e_1 e_0}(t_{23}) \, G_{e_1 g_1}(t_{34}) \, \rho_{g_0 g_0} \right\rangle_{ensemble}. \tag{2}$$

Here, $\langle ... \rangle$ either denotes average of all possible molecular orientations relative to the lab frame, or ensemble energetic averaging over a inhomogeneous distribution of energy gaps in the system. The Green function can be written as $G_{ij}(t) = e^{(-i\omega_{ij} t)}$, where $\omega_{ij} = (E_j - E_i)/\hbar$, $E_{i,j}$ is the energy of the vibrational state i, j. So, the sign of the quantum beat evolution during the pump-probe waiting time T (t_{23} according to the above notation) in the Green's function is opposite in Eq (1) versus Eq (2). The vibrational quantum beat phase on the ground state in the Green's function will be given by $e^{-i\omega_v T}$, whereas it has the opposite phase in the excited state $e^{i\omega_v T}$, where ω_v is the vibrational frequency such that $\omega_v = |\omega_{g_0 g_1}| = |\omega_{e_0 e_1}|$. This fact is utilized in the 2D CM analysis in Section 3 to isolate excited state vibrational quantum beats from those on the ground state. Another important point about the above response function pathways is that the sign of the optical coherences along t_{12} and t_{34} is opposite. This is because the above pathways correspond to rephasing 2D pathways which rephase the dephasing of coherences along t_{12} to lead to a photon echo signal.

In 2D CM analysis, the incoherent population pathways are removed by using a rate model to fit the data. The resulting data only contain contributions from coherent response function pathways such as above. This is followed by Fourier transformation along the t_{23} or T dimension leading to absolute value coherence maps as, $|S_{CM}|$, at a frequency ω_T. It should be noted that, ω_t and ω_τ are the direct Fourier transformed frequency axes resulting from the two interferometric time-delays t_{12} and t_{34}, respectively.

3 Experiment

3.1 Experimental Setup

The schematic of the experimental setup, is shown in Fig 1. The AOPM approach is based on the original work of Tekavec *et al* [15]. Approximately 1µJ, 300 fs pulses centered at 1040 nm from a broadband 1MHz Yb:KGW amplifier are focused on to an 8 mm thick YAG crystal for generation of white light continuum (WLC), which is then routed to two pairs of chirped mirrors for dispersion compensation. The pre-compensated pulses are then split by a 50:50 beamsplitter (BS1), and each portion is routed to two different balanced Mach-Zehnder interferometers, MZ1 and MZ2 as shown in Fig 1. Each arm of the interferometer

is tagged with a unique radio frequency $\omega_{1\text{-}4}$ (for pulse label 1-4 as shown in Fig 1) using acousto-optic modulators (AOMs), which modulate the carrier-envelope phase of the pulse electric field. The phase modulation frequencies for the four arms are denoted as $\Omega_i = 1 - 4$, in accordance with the pulse labels $1 - 4$. The time ordering of the pulses is also shown in the figure along with the corresponding time intervals. Pulse pairs from each MZ are recombined at BS6 to form the third MZ interferometer, such that a collinear pulse train of 4 pulses, each with a unique carrier-envelope phase-shift, originates from BS6 for every laser shot.

As shown in Fig 1, the second port of the beam coming from BS3 in the case of MZ1 and BS5 in MZ2 is sent into the monochromator. The monochromator output pulse is centered at $\omega_{R1;2} = 635$ nm, with a spectral bandwidth of around 1 nm, with corresponding time envelope of ~ 0.6 ps. This ensures approximately constant reference amplitude for the range of time delays t_{12}, and t_{34} scanned in experiment. The probe pulses (output of MZ2) are time-delayed by t_{23} or T before combining with the pump pulse pairs (MZ1) at BS6, as shown in Fig 1. All time delays are controlled by translation stages. Delays are scanned such that time intervals t_{12} and t_{34} are scanned from 0 to 60fs in 2fs steps, and t_{23} or T is scanned from 0 to 3ps in uniform steps for 2D CM scans. The collinear train of four pulses is focussed on the sample of pathlength 100 μm using a Cassegrain telescope with NA = 0.5. Before sending the pulses to the microscope, a 675 nm short-pass filter and a 661 nm long-pass dichroic filter were used. The sample is circulated using a peristaltic pump with no noticeable drop in sample OD through the experiment. The oscillating fluorescence signal, with frequency Ω_- for rephasing and Ω_+ for non-rephasing signals, is passed through the dichroic mirror and a 700 nm long pass filter, and detected using an avalanche photodiode (APD). The collected signal is sent into a lock-in amplifier for phase-sensitive detection. The number of bounces in the chirped mirror pairs was adjusted to compensate the total expected optical dispersion in the setup. Pulse duration of ~ 15 fs was estimated using two-photon autocorrelation signal on a SiC photodiode.

The optically generated reference signals ω_{R1} and ω_{R2} modulate at frequencies Ω_{12} and Ω_{34}. These analog signals are digitized and mixed using a 24-bit audio signal processor to generate reference frequencies $\omega_\pm$. The mixed reference signals are connected as external references to the lock-in amplifier, and the rephasing and non-rephasing signals are detected using these reference signals. Such a detection scheme samples a smaller optical frequency ($\omega_{eg} - \omega_{ref}$) instead of sampling the optical frequency of ω_{eg}, which leads [15] to phase-sensitive lock-in detection. In the experiments, the AOM frequencies are set at $\Omega_1 = 80.109$ MHz, $\Omega_2 = 80.107$ MHz, $\Omega_3 = 80.005$ MHz and $\Omega_4 = 80.0$ MHz through a common clock, such that non-rephasing and rephasing 2D signals oscillate at 7 kHz (Ω_+) and 3 kHz (Ω_-). Modulation at frequencies 7 kHz and 3 kHz can significantly reduce the $1/f$ noise, while the choice of lock-in filter and averaging reduces the white noise. The power on top of the microscope was 30μW for both pump and probe pulses used in the experiment. The total data collection time for each 2D spectrum, including the stage waiting time, is -100 s. Note that $t_{12;34}$ delays are scanned up to only 60 fs because the signal amplitudes are already at the noise floor by that time delay. This implies that frequency resolution in the resulting Fourier transformed 2D spectra will be system limited, since a larger scan range is always possible if the signal did not decay to zero by 60 fs. The experimentally collected time domain data are zero-padded to the $2N$ numbers along both delay axes (t_{12}, t_{34}) before the Fourier transform to get the 2D spectra. N is the total number of collected delay time points.

3.2 Sample Preparation

Oxazine 720 was purchased from M/s Sigma Aldrich and used as such without additional purification. Oxazine stock solutions of optical density (OD) ~ 0.7 – 0.8 in methanol was measured in a 1mm cuvette. A part of this, stock solution was diluted to achieve OD of ~ 0.02 in 100 μm cuvette (concentration: 24 μM) followed by sonication for ~ 30 min to further rule out aggregation. The molecular structure of Oxazine 720 is shown in Fig 2A. The absorption (blue) and fluorescence (red) spectra of Oxazine 720 in methanol are shown in Fig 2B along with the excitation laser spectrum (gray shaded).
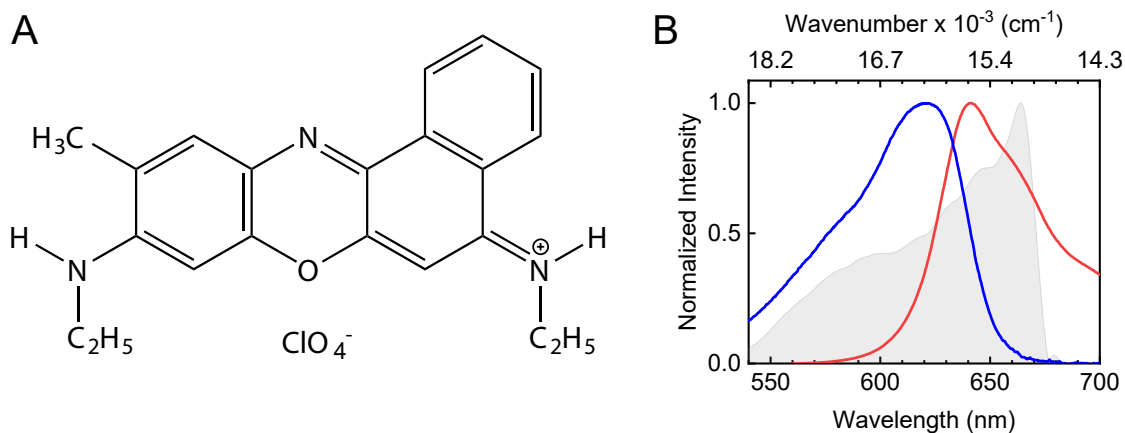
Fig 2. (A) Molecular structure of Oxazine 720 laser dye when it is not dissolved in methanol. (B) Normalized linear absorption (blue) and fluorescence (red) spectra for Oxazine 720 dye in methanol along with the excitation pump spectrum in the gray shaded area.

4 Results and Discussion

Oxazine 720 has ~50 % fluorescence quantum yield [20] in methanol and exhibits solvatochromism with Stoke's shift increasing with solvent polarity. Interestingly, it is reported [20] that dipole moment of Oxazine 720 is substantially increased in the excited state, although Condon approximation is suggested [21] to be valid. Figure 2B shows the normalized linear absorption (blue) and fluorescence (red) spectra of Oxazine 720 along with the laser spectrum. In a polar solvent such as methanol, the ion pair in Oxazine dissociates with a cationic skeleton. From the linear absorption spectrum, the $S_0 \rightarrow S_1$ transition peaks at 618 nm, while the fluorescence spectrum peaks at 640 nm. Rich solvation dynamics is expected and will be a subject of future study from our group. For the subject of the present paper, we are interested in a ~590 cm^{-1} intramolecular FC active vibrational mode of Oxazine 720, which has also been reported previously [22] in 2D measurements, although at an OD which is 10x higher than the present study. This mode and another near 550 cm^{-1} is assigned [23] to phenyl skeletal ring compression and shear vibrations. Turner *et al* have also reported overtones [24] of the latter mode around 1100 cm^{-1} in cresyl violet, another closely related member in the Oxazine family of laser dyes.
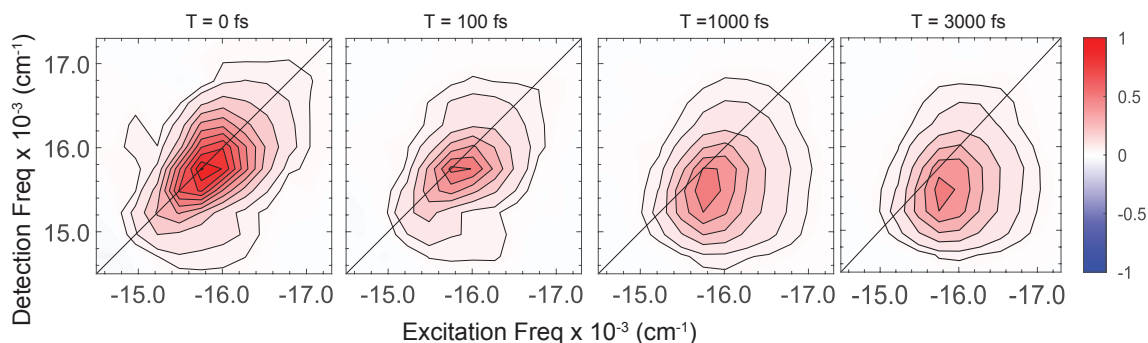
Fig 3. Real absorptive two-dimensional electronic spectra of Oxazine720 in methanol at the pump-probe waiting times: *T* = 0, 100, 1000, 3000 fs, measured with a sample OD of ~20 mOD in 100 μm pathlength. Contours are drawn at the 5%, and 10-100% in 10% intervals for positive or negative contours.
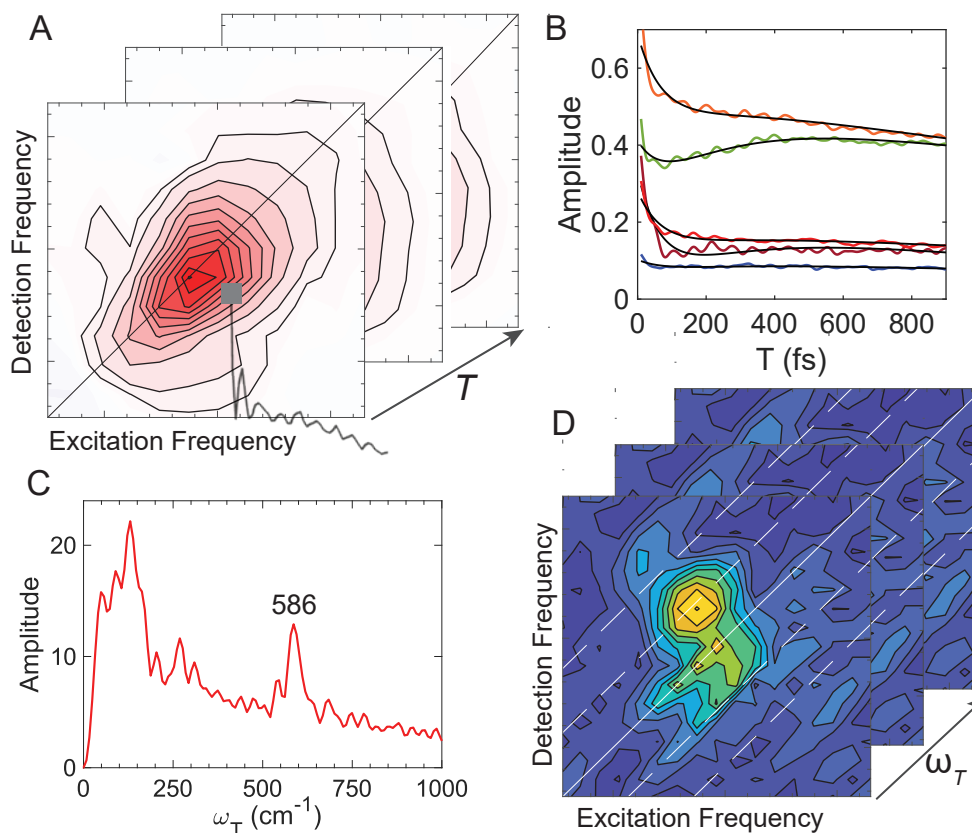
Fig 4. 2D Coherence Maps. (A) Stacked 2D spectra at different pump-probe waiting time T lead to a 3D data set. The gray square is a representative 2D pixel used here to show the equivalent pixel oscillations along T. (B) Fitting each 2D pixel around the 2D maxima along T to a global three exponential rate model to remove the population contributions.(C) Frobenius spectrum obtained from the entire 2D data set after subtracting the global exponential fits followed by Fourier transform of the residuals, and sum over square over excitation and detection frequencies. The strongest frequency in the data corresponds to 586 cm^{-1}, while other less prominent modes are also present although not prominently above the noise floor. (D) After global fitting of each 2D pixel along T, Fourier transform of the residuals leads to coherence maps along the ω_T axis.

Figure 3 shows the absorptive fMES spectra for $T = 0$, 100, 1000 and 3000 fs. The absorptive spectra are phased to obtain real absorptive 2D lineshapes in the relaxed $T = 3$ ps spectrum. Changing slope of the spectrum, from diagonally elongated to circular, and red-shift along the detection axis (Stoke's shift) report on the ultrafast solvation dynamics. Loss of frequency-frequency correlation caused by solvation manifests as change in slope, while red-shift along the detection axis shows the energetic stabilization of the excited electronic state as the solvent shell around the molecule reorients to a change in solute's dipole moment upon electronic excitation. At a longer pump-probe waiting time T, the spectral lineshapes are more rounded than initial T delay spectra, as shown in Fig 3, due to the loss of correlation between excitation and detection frequency axes. This relaxed 2D spectrum can be described [25] as a sample absorption cross-section multiplied by the laser spectrum along the excitation axis and a sum of sample absorption and emission cross-section multiplying the laser spectrum along the detection axis. Figure 3 reports the high signal-to-noise ratio fMES spectra measured at ~ 20 mOD, which is already ~10× lower than the typical OD used in the MES experiment. This highlights the higher sensitivity of fluorescence detection in fMES.High sensitivity of

fluorescence detection has also been utilized by Tokmakoff and co-workers by encoding mid-IR vibrational transitions as electronic transitions [26]. Due to weak Huang-Rhys factor of 0.25 [24] the 0-1 vibrational coherence amplitude for the prominent vibration is expected to be at least ~1/4 weaker than the population signals generated in the experiment. Experimentally, the coherence amplitude is weaker by a factor of 6 (maximum CM amplitude is 0.1538, maximum 2D amplitude is 1). As a measurement of sensitivity, Fig 4 demonstrates coherence map analysis from the prominent vibrational coherence observed at 20 mOD.
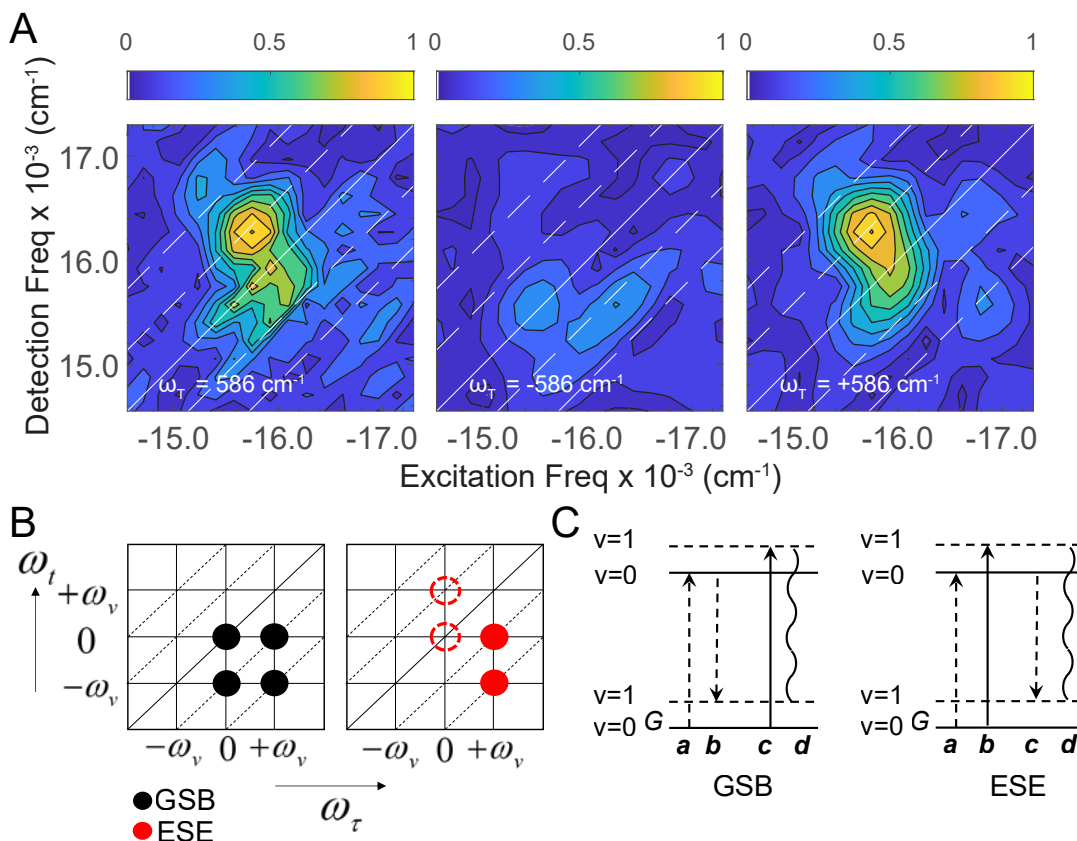
Fig 5. (A) Real rephasing 2D CM (left), the corresponding complex rephasing CMs, $-\omega_T$ (middle) and $+\omega_T$ (right), for ω_T = 586 cm $^{-1}$. This ± separation of the quantum beat separates the excited state coherences from the ground state. The diagonal line in the CMs corresponds to the 2D diagonal and the dashed lines are separated by one quantum of ω_T vibration. Contours are drawn at the 5%, and 10-100% in 10% intervals. The ω_T map is normalized with respect to its corresponding maximum and the $\pm\omega_T$ CMs are normalized with respect to the common maxima of the two CMs. (B) Schematic showing CM contributions expected from GSB (black) and ESE (red) pathways. Contributions with phase $-\omega_T$ are shown as solid, while $+\omega_T$ contributions are shown as dashed circles. (C) Wave mixing diagrams for the oscillatory GSB and ESE signal contributes to the diagonal location of the CM.

The experimentally collected 2D spectra at different pump-probe waiting times *T*, which can be fitted with a global tri-exponential fit along *T* to remove the non-oscillatory population background. The residue of the fit shows the coherent content. The residue is Fourier transformed along *T* to construct the coherent frequency ω_T axis. Slices in the 3D frequency cube along specific ω_T reveals CMs. The CM amplitudes can be explained by Feynman diagram description of the third-order response signals such as those in Eq (1) and Eq (2). The frequency content of the coherence map is summarized in a Frobenius spectrum shown in Fig 4C.

The Frobenius spectrum is defined as $F(\omega_T) = \sum_{\omega\tau} \sum_{\omega\tau} |S(\omega_\tau, \omega_t, \omega_T)|^2$. Note that the sign of the frequency ω_τ is negative for a rephasing signal. Further, if a distinction between GSB and ESE pathways (Eq (1) and Eq (2), respectively) based on the phase of ω_T quantum beat is desired, the starting 2D signal $S(\omega_\tau, \omega_t, \omega_T)$ should be the complex spectrum and not just the real part.

Figure 5 A shows rephasing 2D CMs at $\omega_T = 586$ cm^{-1}. Separation of quantum beat phase into $\pm \omega_T$ are also shown. The coherences contributing to this map correspond to ground and excited state vibrational coherences described by Eq (1) and Eq (2). Figure (5B) shows the expected locations of Feynman pathways leading to ground versus excited state vibrational coherences. Assuming negligible signal contributions from thermally excited vibrational states on the ground electronic state for $\omega_v = 586$ cm^{-1}, it is seen that all coherences with phase $+\omega_T$ arise from excited electronic state vibrational coherences. Coherences with $-\omega_T$ phase arise from ground electronic states on and below the diagonal. It is seen that the ground state vibrational coherences are weaker than those observed on the excited state. This may be because our laser spectrum is strongly biased towards the emission cross-section. As mentioned earlier, coherences at 586 cm^{-1} have been reported earlier [22,27] in conventional 2D measurements. However, the 2D CM analysis presented here at ~10× lower ODs highlights the detection sensitivity of our home-built fMES spectrometer. This is especially significant since our setup is based on a visible white-light continuum where 5% RMS spectral fluctuations across the entire spectral band width are typical [28,29] compared to light sources based on multi-stage optical parametric amplifiers (OPAs) operating in the saturation regime [30].

5 Conclusions

We have described a home-built fMES spectrometer capable of multidimensional spectroscopy with ~10 fs temporal resolution, microscope objective limited spatial resolution, and spectrally decongested system dynamics along three spectral dimensions. Our setup is based on the AOPM approach and uses a visible white-light continuum typically easier to implement than OPAs. We demonstrate the sensitivity of fMES approach by measurements of coherences alongwith the quantum beat phase at ODs nearly an order of magnitude lower than conventional approaches. The isolation of excited state vibrational coherences from the ground state vibrational coherences at low ODs with a sufficient signal-to-noise ratio highlights the power of multidimensional spectroscopy. Future applications of our approach include *in vivo* measurements of energy transfer in photosynthetic systems, energy and charge transfer dynamics in synthetic donor-acceptor systems, and spatially-resolved measurements in photovoltaic materials.

References

1. Jonas D M, Two-Dimensional Femtosecond Spectroscopy, *Annu Rev Phys Chem*, 54(2003)425–463.

2. Jonas D M, Optical Analogs of 2D NMR. *Science*, 300(2003)1515–1517.

3. Aue W P, Bartholdi E, Ernst R R, Two-dimensional spectroscopy. Application to nuclear magnetic resonance, *J Chem Phys*, 64(1976)2229–2246.

4. Cao J, Cogdell R J, Coker D F, Duan H G, Hauer J, Kleinekathöfer U, Jansen T L C, Mančal T, Miller R J D, Ogilvie J P, Prokhorenko V I, Renger T, Tan H-S, Tempelaar R, Thorwart M, Thyrhaug E, Westenhoff S, Zigmantas D, Quantum biology revisited, *Sci Adv*, 6(2020); doi.10.1126/sciadv.aaz4888.

5. Jonas D M, Vibrational and Nonadiabatic Coherence in 2D Electronic Spectroscopy, the Jahn–Teller Effect, and Energy Transfer, *Annu Rev Phys Chem*, 69(2018)327–352.

6. Sio A D, Lienau C,Vibronic coupling inorganic semiconductors for photovoltaics, *Phys ChemChem Phys*, 19(2017)18813–18830.

7. Zhou N, Ouyang Z, Yan L, McNamee M G, You W, Andrew M Moran A M, Elucidation of Quantum-Well-Specific Carrier Mobilitiesin Layered Perovskites, *J Phys Chem Lett*,12(2021)1116–1123.

8. Jones A C, Kearns N M, Ho J-J, Flach J T, Zanni M T, Impact of non- equilibrium molecular packings on singlet fission in microcrystals observed using 2D white-light microscopy. *Nat Chem*, 12(2020)40–47.

9. Dahlberg P D, Ting P-C, Massey S C, Allodi M A, Martin E C, Hunter C N, Engel G S, Mapping the ultrafast flow of harvested solar energy in living photosynthetic cells, *Nat Commun*, 8(2017)988–994.

10. Mohapatra A A, Tiwari V, Patil S, Energy transfer in ternary blend organic solarcells: recent insights and future directions, *Energy Environ Sci*, 14(2021)302–319.

11. Wagner W, Li C, Semmlow J, Warren S, Rapid phase-cycled two- dimensional optical spectroscopy in fluorescence and transmission mode, *Opt Express*,13(2005)3697–3706,

12. Tiwari V, Multidimensional Electronic Spectroscopy in High-Definition-Combining Spectral,Temporal and Spatial Resolutions, *J Chem Phys*, 54(2021)230901; doi.org/10.1063/5.0052234.

13. Draeger S, Roeding S, Brixner T. Rapid-scan coherent 2D fluorescence spectroscopy. *Opt Express*, 25(2017)3259–3267.

14. De A K, Monahan D, Dawlaty J M, Fleming G R, Two-dimensional fluorescence- detected coherent spectroscopy with absolute phasing by confocal imaging of a dynamic grating and 27-step phase-cycling, *J Chem Phys*, 140(2014)194201; doi.org/10.1063/1.4874697.

15. Tekavec P F, Lott G A, Marcus A H, Fluorescence-detected two-dimensional electronic coherence spectroscopy by acousto-optic phase modulation, *J Chem Phys*,127(2007)214307–214327.

16. Goetz S, Donghai Li, Kolb V, Pflaum J, Brixner T, Coherent two-dimensional fluorescence micro-spectroscopy, *Opt Express*, 26(2018)3915–3925.

17. Tiwari V, Matutes Y A, Gardiner A T, Jansen T L C, Cogdell R J, Ogilvie J P, Spatially resolved fluorescence-detected two-dimensional electronic spectroscopy probes varying excitonic structure in photosynthetic bacteria, *Nat Commun*, 9(2018)4219; doi.org/10.1038/s41467-018-06619-x.

18. Scherer N F, Carlson R J, Matro A, Du M, Ruggiero A J, Romero-Rochin V, Cina J A, Fleming G R, Rice S A, Fluorescence-detected wavepacket interferometry: Time resolved molecular spectroscopy with sequences of femtosecond phase-locked pulses, *J Chem Phys*, 95(1991)1487–1511.

19. Cina J A, Wave-Packet Interferometry and Molecular State Reconstruction: spectroscopic Adventures on the Left-Hand Side of the Schrödinger Equation, *Annu Rev Phys Chem*, 59(2008)319–342.

20. Zakerhamidi M S, Sorkhabi S G, Solvent effects on the molecular resonance structures and photo-physical properties of a group of oxazine dyes, *J Lumin*, 157(2015)220–228.

21. Vogel M, Rettig W, Fiedeldei U, Baumgärtel H, Non-radiative deactivation via biradicaloid charge-transfer states in oxazine and thiazine dyes, *Chem Phys Lett*, 148(1988)347–352.

22. Zhu R, Zou J, Wang Z, Chen H, Weng Y, Electronic State-Resolved Multimode-Coupled Vibrational Wavepackets in Oxazine 720 by Two-Dimensional Electronic Spectroscopy, *J Phys Chem A*, 124(2020)9333–9342.

23. Kostjukov V V, Photoexcitation of oxazine170 dye in aqueous solution:TD-DFT study, *J Mol Model*, 27(2021)311; doi. org/10.1007/s00894-021-04931-w.

24. Barclay M S, Huff J S, Pensack R D, Davis P H, Knowlton W B, Yurke B, Dean J C, Arpin P C, Turner D B, Characterizing Mode Anharmonicity and Huang–Rhys Factors Using Models of Femtosecond Coherence Spectra, *J Phys Chem Lett*, 13(2022)5413–5423.

25. Hybl J D, Ferro A A, Jonas D M, Two-dimensional Fourier transform electronic spectroscopy, *J Chem Phys*, 115(2001)6606–6622.

26. Whaley-Mayda L, Guha A, Penwell S B, Tokmakoff A, Fluorescence-encoded infrared vibrational spectroscopy with single-molecule sensitivity, *J Am Chem Soc*, 143(2021)3060–3064.

27. Carbery W P, Pinto-Pacheco B, Buccella D, Turner D B, Resolving the fluorescence quenching mechanism of an oxazine dye using ultrabroadband two-dimensional electronic spectroscopy, *J Phys Chem A*,123(2019)5072–5080.

28. Dobryakov A L, Kovalenko S A, Weigel A, Pérez-Lustres J L, Lange J, Müller A, Ernsting N P, Femtosecond pump/supercontinuum-probe spectroscopy: Optimized setup and signal analysis for single-shot spectral referencing, *Rev Sci Instrum*, 81(2010)113106; doi.org/10.1063/1.3492897.

29. Bradler M, Baum P, Riedle E, Femtosecond continuum generation in bulk laserhost materials with sub-mJ pump pulses, *Appl Phys B*, 97(2009)561–574.

30. Moses J, Huang S.-W, Hong K.-H, Mücke O D, Falcão-Filho E L, Benedick A, Ilday F O, Dergachev A, Bolger J A, Eggleton B J, Kärtner F X, Highly stable ultrabroadband mid-IR optical parametric chirped-pulse amplifier ptimizedperce pression, *Opt Lett*, 34(2009)1639–1641.

Amitav Sahu is a Ph D scholar in the group of Prof Vivek Tiwari at the Indian Institute of Science, Bangalore, India. He received his master's degree in Physics from North Orissa University, Odisha, India. His current research mainly focuses on developing coherent multidimensional electronic spectroscopic methods to probe ultrafast energy and charge transfer mechanisms in photosynthetic systems, organic polymers, and singlet fission materials. Parallelly, he also involves in developing theoretical models to understand the interplay of vibrational and electronic motions which drive these ultrafast processes.

Vivek Nagendra Bhat is a Ph D student working with Prof Vivek Tiwari at the Indian Institute of Science, Bangalore, India. He did his undergraduate at M M Arts and Science College Sirsi, Karnataka, and completed his M Sc Physics in Department of Physics, Karnatak University Dharwad. His current research mainly focuses on developing high throughput femtosecond pump-probe and coherent multidimensional spectroscopic methods.

Sanjoy Patra is an Integrated Ph D student working with Prof Vivek Tiwari at the Indian Institute of Science, Bangalore, India. He did his undergraduate in 2018 at Ramakrishna Mission Residential College, Narendrapur, West Bengal. His current research mainly focuses on theoretically modeling ultrafast energy/charge transfer systems to better understand the mechanisms involved in such processes. In parallel, he is also developing Fluorescence-detected Multidimensional Electronic Spectroscopy (fMES) methods to probe quantum dynamics of excitons.

Vivek Tiwari is an Assistant Professor at Indian Institute of Science, Bangalore. He completed his Ph D in Chemical Physics at the University of Colorado Boulder under the supervision of Prof David Jonas in the year 2014. Vivek conducted his postdoctoral work in the group of Prof Jennifer Ogilvie at the University of Michigan. His research group in IISc started in the year 2019 and focuses on understanding the interplay of vibrational and electronic motions which drive ultrafast energy and charge delocalization. To this end, his research group develops multidimensional spectroscopic techniques and theoretical models to probe the above physics is natural and artificial light-harvesting systems.